RESEARCH ARTICLE

National Science Review
5: 895–906, 2018
doi: 10.1093/nsr/nwy065
Advance access publication 28 June 2018

CHEMISTRY

Surface engineering at the interface of core/shell nanoparticles promotes hydrogen peroxide generation

Yonggang Feng[1], Qi Shao[1], Bolong Huang[2], Junbo Zhang[1] and Xiaoqing Huang[1,*]

ABSTRACT

Hydrogen peroxide (H_2O_2), an environmentally friendly oxidant, has already been widely used in many chemical synthesis and industrials as an alternative to replace traditional oxidants including chlorinated oxidizers and strong acids. However, the conventional synthesis method confronts intense energy cost, tedious separation procedures and high cost, which is not competitive with traditional oxidants. Although direct H_2O_2 synthesis from H_2 and O_2 is a green and atomically economic reaction, satisfactory activity and desirable selectivity still remain formidable challenges. Herein, for the first time, a class of Pd@NiO-x nanoparticles (NPs) (x = 1, 2, 3 and 4) with a unique core@shell interface structure has been created to achieve high activity, selectivity and stability for the direct H_2O_2 synthesis. A precise thermal annealing on Pd@Ni-x NPs revealed that the resulting Pd@NiO-x NPs exhibited the volcano-like activity toward direct H_2O_2 synthesis as a function of annealing temperature and time. By tuning the composition of Pd@NiO-x NPs and the reaction condition, the efficiency of H_2O_2 synthesis could be well optimized with 5 wt% Pd@NiO-3/TiO_2 exhibiting the highest productivity (89 mol/(kg_{cat} h)) and selectivity (91%) to H_2O_2 as well as excellent stability, making it one of the best catalysts for direct H_2O_2 synthesis reported to date.

Keywords: hydrogen peroxide, direct synthesis, Core@shell structure, palladium, nickel oxide

INTRODUCTION

Hydrogen peroxide (H_2O_2) is a versatile chemical in modern industry, widely applied in the bleaching of textiles and pulp, treatment of waste water, removal of organic pollutant and chemical synthesis, etc. [1–5]. To date, H_2O_2 has been industrially manufactured using an indirect process that involves the sequential hydrogenation and oxidation of alkyl anthraquinone, which is, however, a multi-step process with high cost and is energy-intensive [6,7]. In sharp contrast, due to the remarkable advantages of atom economy, low energy consumption and only by-product of H_2O, the direct synthesis of H_2O_2 from H_2 and O_2 is expected to be the most efficient way to produce H_2O_2 [7]. To date, the direct synthetic route has mainly been achieved by supported Pd-based catalysts [8–10]. The major problem associated with that is related to the low selectivity of H_2O_2, since Pd is also very active for side reactions, such as the decomposition and hydrogenation of H_2O_2 as well as the formation of H_2O [9]. Adding a large amount of strong acid or halide promoters to the reaction medium is one solution to achieve high selectivity for H_2O_2 generation via suppressing the side reactions. However, it also leads to metal leaching and requires further purification of H_2O_2 products [10,11]. Recently, Pd–Au nanocatalysts have been demonstrated to have enhanced overall activity mainly due to the alloy effect and the presence of strong acid or halide promoters [8,12,13]. This has accordingly stimulated extensive research to explore the promotional effect by introducing Au, Pt, Ru and Ag into the Pd-based catalysts [14–20]. Without the use of halides, a Pd–Sn catalyst has achieved high H_2O_2 selectivity by creating a tin oxide surface layer onto small Pd-rich particles for preventing the over-hydrogenation and decomposition of H_2O_2 [21]. Despite great efforts being devoted to constructing Pd-based catalysts by introducing second metals, understanding high-performance Pd-based catalysts for direct H_2O_2 generation from either deep characterization or theoretical investigation is still extremely limited.

It is considered that the intrinsic surface property of Pd-based catalysts is essential for the

[1]College of Chemistry, Chemical Engineering and Materials Science, Soochow University, Suzhou 215123, China and [2]Department of Applied Biology and Chemical Technology, Hong Kong Polytechnic University, Hong Kong, China

*Corresponding author. E-mail: hxq006@suda.edu.cn

Received 20 April 2018; **Revised** 28 May 2018; **Accepted** 26 June 2018

selectivity and activity of direct H_2O_2 synthesis. This arises because the barrier for O–O bond scission is sensitive to the Pd surface structure, the key parameter governing H_2O_2 synthesis and decomposition activity [22]. The oxidized Pd surface (Pd–O) bonding is more selective but less active towards the H_2O_2 synthesis than the metallic Pd, mostly attributed to the higher propensity of H_2O_2 to be absorbed on the metallic Pd surface than the Pd–O surface [21–23]. Therefore, it is anticipated that controlling the surface oxidation state of the Pd-based catalysts can be an effective route to regulating their catalytic properties, while precise surface tuning is extremely hard for the Pd-based catalysts due to their obvious tendency for thermal agglomeration or thermal morphology transformation.

We proposed that the aforementioned challenges can be overcome by simultaneous surface and interface modulations via constructing a core@shell structure, such as encapsulating Pd nanocrystals (NCs) with a shell [24,25]. To this end, herein we report the design of a class of Pd core-porous NiO shell catalysts in which the porous NiO shell is highly beneficial in protecting Pd NPs from aggregation during the reaction process as well as providing pore paths to allow the reactant gases to reach the Pd core and to further explore the correlations between the catalytic efficiency and the surface structural features. As a consequence, the supported Pd@NiO-x core–shell NPs were found to be a class of highly active, selective and stable catalysts towards direct H_2O_2 synthesis from H_2 and O_2. These Pd@NiO-x NPs with a unique core–shell interface structure were created by direct thermal annealing of Pd@Ni-x NPs with precise annealing temperature and time. By optimizing the Pd/Ni ratio as well as reaction conditions, 5 wt% Pd@NiO-3/TiO_2 performed the highest selectivity to H_2O_2 of 91%, the highest activity of 89 mol/(kg_{cat} h), as well as excellent stability. The X-ray photoelectron spectroscopy (XPS) results demonstrated that the surface of the Pd core was partially oxidized, revealing that the active metallic Pd core is co-modified by Pd^{2+} and NiO, which is effective to abate side reactions. Moreover, the first-principles simulations further interpreted the mechanism from both electronic and energetic views, which confirmed that the presence of a unique interface structure with cavities in Pd@NiO NPs guarantees the high selectivity of direct H_2O_2 synthesis.

RESULTS AND DISCUSSION

The Pd@Ni-x NPs (x = 1, 2, 3 and 4) with tunable compositions were first prepared through a facile solvothermal approach. They are highly monodisperse and employ the obvious core/shell structure (Supplementary Fig. 1, available as Supplementary Data at *NSR* online). The obtained Pd/Ni-x NPs were further loaded onto commercial TiO_2 (P25) to make Pd@Ni-x/TiO_2 catalysts with a total Pd content of 5 wt%, as determined by inductively coupled plasma mass spectroscopy (ICP-MS). The Pd@Ni-3/TiO_2 catalysts were further characterized by transmission electron microscopy (TEM), high-angle annular dark-field scanning transmission electron microscopy (HAADF-STEM), STEM-energy dispersive X-ray spectroscopy (EDS) elemental mapping and EDS line-scan analysis. TEM imaging reveals that Pd@Ni-3 NP supported on TiO_2 has a diameter of ∼22 nm (Fig. 1a and b). The STEM-EDS elemental mappings reveal that Ni presents as a thick shell (∼5 nm) coated on a Pd core (∼17 nm) (Fig. 1c and d), consistently with the powder X-ray diffraction (PXRD) results that both the face-centered cubic (*fcc*) Pd (JCPDS no. 87–0638) and *fcc* Ni (JCPDS no. 89–7128) observed in the Pd@Ni-3 NPs/TiO_2 (Fig. 2a and b). In the very first attempt, we directly applied the Pd@Ni-x/TiO_2 catalysts for direct H_2O_2 synthesis. As shown in Supplementary Table 1, available as Supplementary Data at *NSR* online, the H_2O_2 productivity of these 5 wt% Pd@Ni-x/TiO_2 (x = 1, 2, 3 and 4) catalysts are calculated to be only 1.4, 1.0, 1.0 and 0.8 mol/(kg_{cat} h), respectively. Since Pd is considered to be the active element for direct H_2O_2 synthesis, we ascribe the low activity of these Pd/Ni core/shell catalysts toward H_2O_2 synthesis to the thick Ni shell, by which the activity of Pd is heavily blocked.

To this end, to enhance the H_2O_2 productivity of these Pd@Ni-x/TiO_2 catalysts, exposing the active Pd sites in the Pd core to effectively access H_2 and O_2 is highly desirable. Since NiO has the nature of a porous structure, which can be made through a simple oxidation treatment [26–29], we calcined the 5 wt% Pd@Ni-3/TiO_2 catalyst in air. After thermal treatment, we measured the activities of these catalysts toward direct H_2O_2 synthesis. As shown in Supplementary Table 2, available as Supplementary Data at *NSR* online, after being calcined at 250°C for 1 h, 5 wt% Pd@Ni-3/TiO_2 exhibits H_2O_2 productivity of 14 mol/(kg_{cat} h). Once the calcined temperature was raised to 300°C, the H_2O_2 productivity increased to 46 mol/(kg_{cat} h). We also tested the H_2O_2 productivity by prolonging the reaction time to 1 h for annihilating the negative influence on the diffusion rates of O_2 and H_2 due to the thick NiO shell newly formed. As expected, the H_2O_2 productivity of the 5 wt% Pd@Ni-3/TiO_2 calcined at 250°C for 1 h increased sharply to 89 mol/(kg_{cat} h). Nevertheless, the 5 wt%

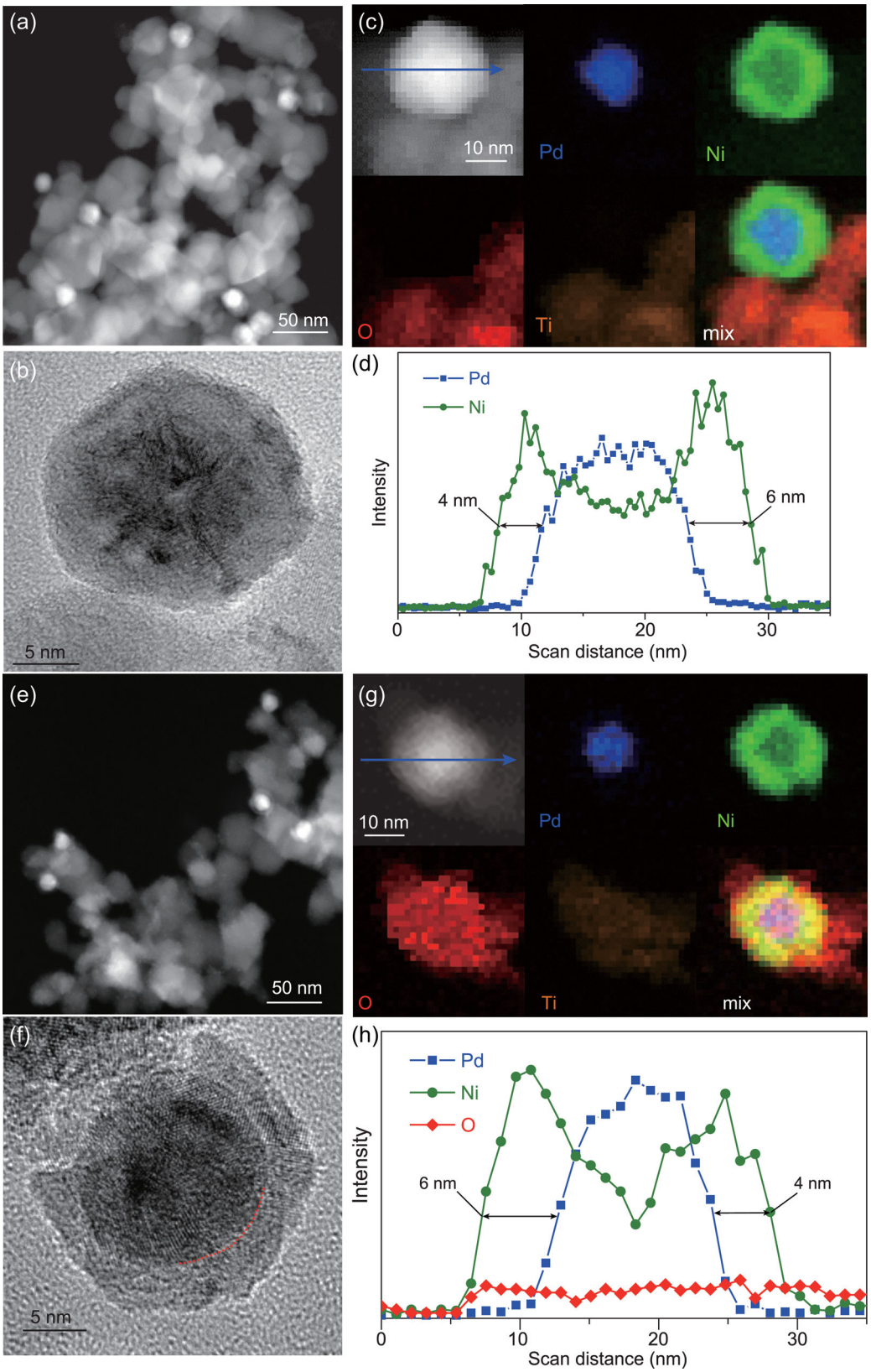

Figure 1. Structural and compositional characterizations of Pd@Ni-3/TiO_2 and Pd@NiO-3/TiO_2. (a) and (e) Low-magnification HAADF-STEM images; (b) and (f) high-magnification TEM images; (c) and (g) HAADF-STEM images and corresponding elemental mappings of (a), (b) and (c) 5 wt% Pd@Ni-3/TiO_2 and (e), (f), (g) and (f) 5 wt% Pd@NiO-3/TiO_2, respectively. EDS line-scan analysis of (d) 5 wt% Pd@Ni-3/TiO_2 and (h) 5 wt% Pd@NiO-3/TiO_2 across the blue arrow in the insets of (c) and (g), respectively. The red dotted line in (f) indicates the interface structure between the Pd core and the NiO shell.

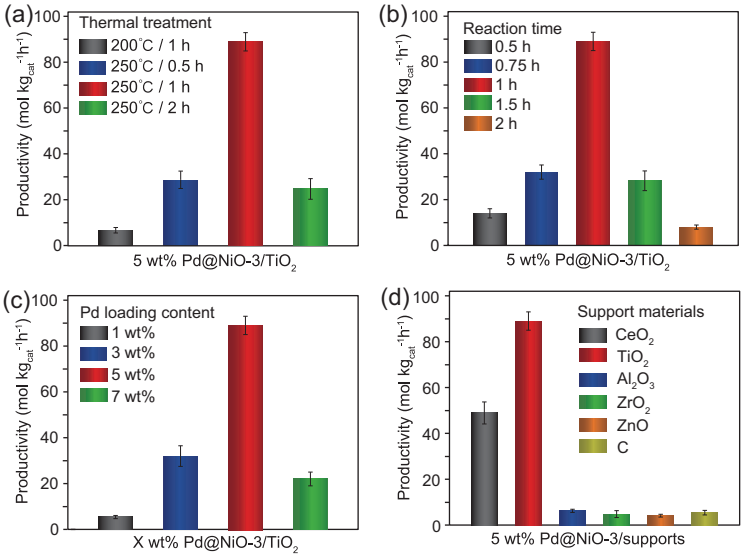

Figure 2. The optimization of catalysts and reaction conditions. The optimization of catalysts for achieving high H_2O_2 productivity. The effects of (a) thermal treatment with different temperature and calcined time, (b) the reaction time, (c) the Pd loadings and (d) the support materials for the direct H_2O_2 synthesis.

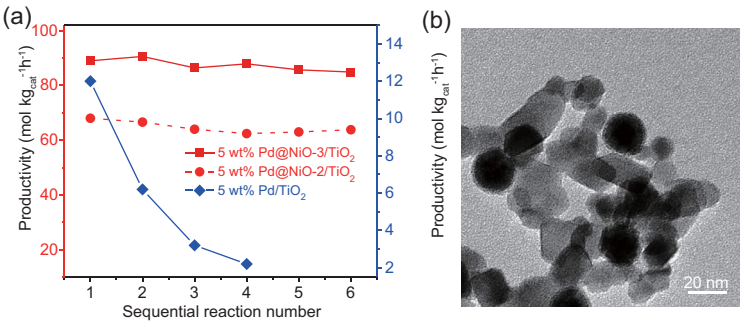

Figure 3. The productivity of sequential H_2O_2 synthesis and TEM image after sequential H_2O_2 synthesis. (a) Sequential H_2O_2 synthesis reactions over 5 wt% Pd@NiO-2/TiO_2, 5 wt% Pd@NiO-3/TiO_2 and 5 wt% Pd/TiO_2. (b) TEM image of 5 wt% Pd@NiO-3/TiO_2 after sequential H_2O_2 synthesis.

Pd@Ni-3/TiO_2 that calcined at 300°C for 1 h reduced dramatically to 4 mol/(kg_{cat} h). In order to figure out the interesting observations, detailed characterizations of the 5 wt% Pd@Ni-3/TiO_2 calcined at 250 and 300°C were carried out.

The reason for the significantly different catalytic activity of 5 wt% Pd@Ni-3/TiO_2 catalysts calcined at 250 and 300°C was first characterized by TEM. Supplementary Fig. 3a, available as Supplementary Data at *NSR* online, clearly shows that the intermediate void was formed when the 5 wt% Pd@Ni-3/TiO_2 was calcined at 300°C for 1 h. The formation of a NiO shell was confirmed by STEM-EDS elemental mappings (Fig. 3b). When it was calcined at 250°C for 1 h, the distinct interface structure between the Pd core and the porous NiO shell was clearly observed (Fig. 1e and f). The element distribution was also invested by STEM-EDS elemental mappings and EDS line-scan analysis, where the Pd core was encapsulated by the NiO shell (Fig. 1c, d, g and h). Therefore, these two different catalysts were denoted as 5 wt% Pd@void@NiO-3/TiO_2 and 5 wt% Pd@NiO-3/TiO_2, respectively. In the thermal treatment, the pristine Ni shell was exposed to oxygen so that the porous NiO shell was formed as a priority. When outward diffusion of the Ni is faster than the inward diffusion of the Ni at the elevated temperature, the void appears at the inside of the core/shell interface and then grows up until the hollow interior structure forms due to the Kirkendall effect [30–33].

The creation of a porous NiO shell is beneficial for exposing Pd active sites and thus enhancing the productivity of H_2O_2 as the reaction time is prolonging to 1 h (Supplementary Table 1, entry 3 and Supplementary Table 2, entry 2, available as Supplementary Data at *NSR* online). Noticeably, the H_2O_2 hydrogenation activity of 5 wt% Pd@NiO-3/TiO_2 was much lower than that of 5 wt% Pd@void@NiO-3/TiO_2 (Supplementary Table 2, entries 2 and 4, available as Supplementary Data at *NSR* online). Compared with 5 wt% Pd@NiO-3/TiO_2, the void space in 5 wt% Pd@void@NiO-3/TiO_2 is beneficial to expose more of the Pd core surface, but hardly any contact interface between the Pd core and the NiO shell, which can be highly active for H_2O_2 synthesis and but also highly active for its subsequent hydrogenation and decomposition. Therefore, 5 wt% Pd@void@NiO-3/TiO_2 exhibits high activity for H_2O_2 degradation as well as favoring a short reaction time for higher H_2O_2 productivity (Supplementary Table 2, entries 3 and 4, available as Supplementary Data at *NSR* online). From the significantly different performances between 5 wt% Pd@NiO-3/TiO_2 and 5 wt% Pd@void@NiO-3/TiO_2, it is apparent that the created interface structure between the Pd core and the NiO shell is essential to promote productivity and low hydrogenation activity.

To further evaluate the correlation between the NiO shell and its catalytic performance, other Pd@NiO-x/TiO_2 (x = 1, 2 and 4) were also prepared by the same thermal treatment as executed on the 5 wt% Pd@Ni-3/TiO_2. The STEM-EDS elemental mappings and EDS line-scan analysis show that the thickness of the NiO shell increased from ~2 to ~7 nm as the Ni content increased (Supplementary Figs 4–6, available as Supplementary Data at *NSR* online). In addition, 5 wt% Pd/TiO_2 without the NiO shell was also prepared for H_2O_2 synthesis through acid etching of 5 wt% Pd@Ni-3/TiO_2 (details in Supporting Information). The TEM image shows that the size of the NPs decreases to

Table 1. Direct H_2O_2 synthesis and selectivity results of 5 wt% Pd@NiO-x/TiO_2.

Entry	Catalyst	H_2O_2 productivity (mol/(kg_{cat} h))	H_2O_2 selectivity (%)
1	5 wt% Pd@NiO-1/TiO_2	28	62
2	5 wt% Pd@NiO-2/TiO_2	68	82
3	5 wt% Pd@NiO-3/TiO_2	89	91
4	5 wt% Pd@NiO-4/TiO_2	44	75
5	5 wt% Pd/TiO_2	12	41

All catalysts were calcined in air at 250°C for 1 h before catalytic investigations. H_2O_2 productivity was determined under the following reaction conditions: 5% H_2/N_2 (3.6 MPa) and 99% O_2 (0.4 MPa), 8.5 g solvent (2.9 g HPLC water, 5.6 g MeOH), 0.0025 g catalyst, 2°C, 1200 rpm and 1 h.

around 15 nm due to the removal of the NiO shell (Supplementary Fig. 7a, available as Supplementary Data at *NSR* online). The STEM-EDS elemental mappings and EDS line-scan analysis show a very strong Pd signal but negligible Ni signal, confirming that the Ni shell was removed by the acid (Supplementary Fig. 7c, d available as Supplementary Data at *NSR* online). As shown in Table 1, 5 wt% Pd/TiO_2 exhibits rather low productivity (12 mol/(kg_{cat} h)) and selectivity (41%) relative to Pd@NiO-x/TiO_2 catalysts, indicating that the NiO shell plays a significant role in promoting the catalytic performance of H_2O_2 synthesis. Moreover, among the 5 wt% Pd@NiO-x/TiO_2 catalysts, 5 wt% Pd@NiO-3/TiO_2 exhibits improved H_2O_2 productivity and the best selectivity over 5 wt% Pd@NiO-1/TiO_2 and 5 wt% Pd@NiO-2/TiO_2. Unexpectedly, the catalytic performance was not improved as the NiO shell thickness further increased. The 5 wt% Pd@NiO-4/TiO_2 displays relatively lower H_2O_2 productivity and selectivity than the 5 wt% Pd@NiO-3/TiO_2 even if it has the thickest NiO shell. Furthermore, these catalysts were also tested for H_2O_2 hydrogenation with varying concentrations of H_2O_2. As shown in Supplementary Table 3, available as Supplementary Data at *NSR* online, 5 wt% Pd/TiO_2 shows much higher H_2O_2 hydrogenation activity than 5 wt% Pd@NiO-x/TiO_2 catalysts due to the loss of the NiO shell. Noticeably, 5 wt% Pd@NiO-3/TiO_2 shows no hydrogenation activity in a low concentration of H_2O_2 (2 wt%), whereas 5 wt% Pd@NiO-1/TiO_2 and 5 wt% Pd@NiO-2/TiO_2 show substantially higher H_2O_2 degradation activity at all concentrations studied. Especially, the H_2O_2 hydrogenation of 5 wt% Pd@NiO-4/TiO_2 is relatively higher than that of 5 wt% Pd@NiO-3/TiO_2. From the above results, we can conclude that the catalytic performance of 5 wt% Pd@NiO-x/TiO_2 is not proportional to the NiO thickness. Because metallic Pd is more effective for H_2O_2 synthesis and hydrogenation than oxidized Pd, the surface feature of the catalyst, in particular the oxidation state of the active core, plays a crucial role in obtaining high selectivity as well as activity. Therefore, it is reasonable to speculate that, in addition to the thickness effect of the NiO shell, there should be subtle differences on the Pd core surface of different 5 wt% Pd@NiO-x/TiO_2 (x = 1, 2, 3 and 4).

Hence, the surface structures of all these catalysts were further analysed by XPS (Supplementary Table 4, available as Supplementary Data at *NSR* online). XPS spectra of the pristine 5 wt% Pd@Ni-x/TiO_2 reveal that the Ni content on the surface is very high, with only metallic Pd observed (Supplementary Table 4, entries 1–4, available as Supplementary Data at *NSR* online). After thermal treatment, Ni is still the dominating surface species in 5 wt% Pd@NiO-x/TiO_2 but the Pd/Ni ratio decreases obviously in 5 wt% Pd@NiO-3/TiO_2 and 5 wt% Pd@NiO-4/TiO_2, due to the formation of a thicker NiO shell. In addition, Pd^{2+} is observed in all the Pd@NiO-x/TiO_2, although Pd^0 is still the major form after thermal treatment (Supplementary Table 4, entries 5–8, available as Supplementary Data at *NSR* online). It is worth noting that the Pd^0/Pd^{2+} ratio of 5 wt% Pd@NiO-x/TiO_2 (x = 1, 2 and 3) is about 3 (Supplementary Table 4, entries 5–7, available as Supplementary Data at *NSR* online). However, it is close to 9 in 5 wt% Pd@NiO-4/TiO_2 (Supplementary Table 4, entry 8, available as Supplementary Data at *NSR* online), ascribed to the thick NiO shell that hinders the oxidation of the Pd core during thermal treatment. In addition, Pd^{2+} is regarded as more selective but less active towards H_2O_2 synthesis than that of the metallic Pd due to the low propensity of H_2O_2 on Pd^{2+}. From the above evidence, the reduced percentage of Pd^{2+} on the surface of the Pd core can be responsible for the lowest catalytic performance of 5 wt% Pd@NiO-4/TiO_2 among the different 5 wt% Pd@NiO-x/TiO_2 catalysts. Therefore, in the Pd@NiO-x/TiO_2 system, the unique interface structure with the appropriate Pd^0/Pd^{2+} ratio and the desirable NiO shell, which make the active metallic Pd core co-modified by Pd^{2+} and NiO, is essential to improve catalytic performance for the direct synthesis of H_2O_2 (Scheme 1).

To this end, we further optimized the conditions for direct H_2O_2 synthesis by tuning the different parameters, such as thermal treatment, reaction time, mass loading, as well as support. As shown in Fig. 2, when the calcined temperature decreased to 200°C for 1 h, 5 wt% Pd@NiO-3/TiO_2 exhibits lower productivity (7 mol/(kg_{cat} h)) than that at 250°C for 1 h (89 mol/(kg_{cat} h)). The productivity of H_2O_2 was not improved by changing the calcined time to

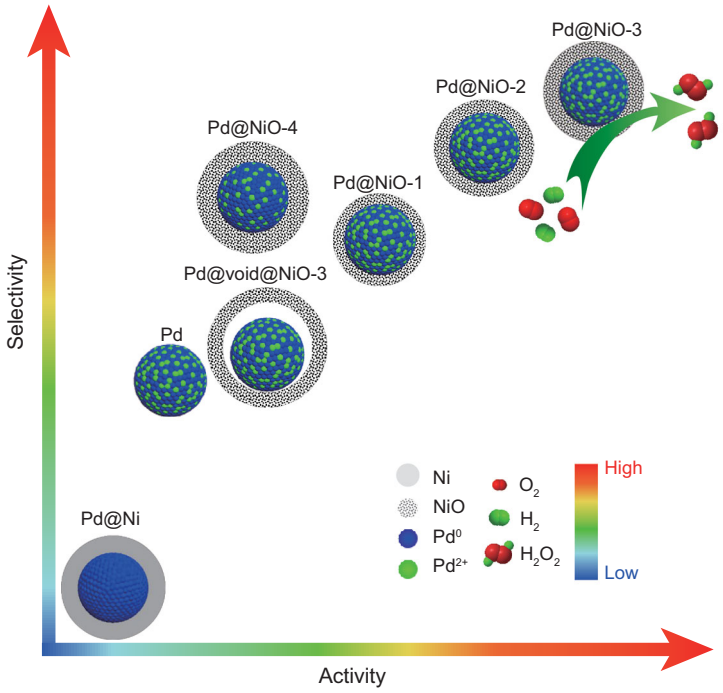

Scheme 1. Schematic illustration showing the activity and selectivity toward H_2O_2 synthesis of 5 wt% Pd@Ni-3/TiO_2, 5 wt% Pd@NiO-x/TiO_2 (x = 1, 2, 3 and 4), 5 wt% Pd@void@Ni-3/TiO_2 and 5 wt% Pd/TiO_2.

0.5 h (29 mol/(kg_{cat} h)) and 2 h (25 mol/(kg_{cat} h)) (Fig. 2a). The reaction time of the direct H_2O_2 synthesis is another critical factor. When the reaction time changes from 0.5 to 2 h, the productivity of H_2O_2 exhibits a volcano shape. When the reaction time reaches 1 h, the 5 wt% Pd@NiO-3/TiO_2 exhibits the best productivity of H_2O_2 (Fig. 2b). Moreover, Pd loading was also taken into consideration, which shows that the 5 wt% Pd loading is better than that of the 1 (5 mol/(kg_{cat} h)), 3 (32 mol/(kg_{cat} h)) and 7 wt% (22 mol/(kg_{cat} h)) (Fig. 2c). In direct H_2O_2 synthesis, the support is another key factor that affects the catalytic performance. Therefore, we also prepared different 5 wt% Pd@NiO-3/supports for direct H_2O_2 synthesis (Supplementary Fig. 8, available as Supplementary Data at *NSR* online). We can see that, besides TiO_2, CeO_2 (49 mol/(kg_{cat} h)) also exhibits relatively high activity for H_2O_2 direct synthesis, while the other supports, such as Al_2O_3 (6.2 mol/(kg_{cat} h)), ZrO_2 (4.8 mol/(kg_{cat} h)), ZnO (4.1 mol/(kg_{cat} h)) and C (5.4 mol/(kg_{cat} h)) (Fig. 2d), are not suitable for this Pd-NiO system toward direct H_2O_2 synthesis.

The catalytic durability of 5 wt% Pd@NiO-x/TiO_2 (x = 2 and 3) and 5 wt% Pd/TiO_2 was also evaluated. After running the reaction for six cycles, we found that 5 wt% Pd@NiO-x/TiO_2 can retain high productivity for direct H_2O_2 synthesis, while the 5 wt% Pd/TiO_2 lost most of its H_2O_2 productivity after four cycles (Fig. 3a). The excellent recycle stability of 5 wt% Pd@NiO-x/TiO_2 can be by virtue of the encapsulation of the Pd core by the NiO shell, which immobilizes the Pd core. In contrast, the low stability of 5 wt% Pd/TiO_2 is probably due to the lack of a unique interface structure between the Pd core and the NiO shell, which inevitably results in leaching and/or aggregation of Pd NPs during the reaction cycles. To verify this assumption, ICP-MS was carried out to determine the Pd content variation of 5 wt% Pd@NiO-3/TiO_2 and 5 wt% Pd/TiO_2 after cycles. The results show negligible loss of Pd (4 ppb) of 5 wt% Pd@NiO-3/TiO_2 after six cycles, implying nearly no variation in the composition of 5 wt% Pd@NiO-3/TiO_2, while a high amount of Pd leaching (2 ppm) occurred on 5 wt% Pd/TiO_2. This observation was also confirmed by the TEM images and EDS of these catalysts after reaction cycles, where the morphology and compositions of 5 wt% Pd@NiO-2/TiO_2 and 5 wt% Pd@NiO-3/TiO_2 were largely maintained while the aggregated feature was observed for 5 wt% Pd/TiO_2 (Fig. 3b and Supplementary Fig. 9, available as Supplementary Data at *NSR* online).

To simulate the proposed catalytic reaction of H_2O_2 synthesis, we built the local interface (IF) structure of the Pd/NiO (core/shell) system with bonding along the (100) surface for a simplified straightforward illustration (Fig. 4a). The *fcc*-Pd and rocksalt NiO (simple cubic) have the least lattice mismatch on the (100) surface of each other. The Pd sites at the interface are bonded with O epitaxially expanded from the NiO shell layer. The interface without a cavity is an anisotropic metallic system exhibiting anti-bonding orbitals while the NiO and Pd layers present bonding orbitals, respectively (Fig. 4b). The Pd-4d orbital levels are predominantly covering the highest occupied bands near the Fermi level (E_F, 0 eV), implying a high tendency to be electron-rich and more active in transfer. Moreover, the difference of d-orbital levels has indeed reflected the differentiation of electronic activity (Fig. 4c) between Pd and Ni sites from the bulk and interface (IF), respectively, which means the interfacial homogenization of the *d*-electron distribution has been inhibited. The peak of the Pd-4d orbital at the IF is obviously lower than those in the bulk, indicating that the activity of the Pd-4d-electrons at the interface has been suppressed by the presence of the O-sites via interfacing over-coordinated Pd–O bonding. In line with experimental observation, the choice of porous NiO is understandable, as NiO with a cavity or wall in the local morphology can exhibit more selectivity to form intermediate Ni-(O–O)* (* denotes the absorbing state) bonding without O–O cleavage, and is more energetically favorable to the Pd-(O–O)*. Therefore, it is necessary to further investigate the IF with a NiO cavity

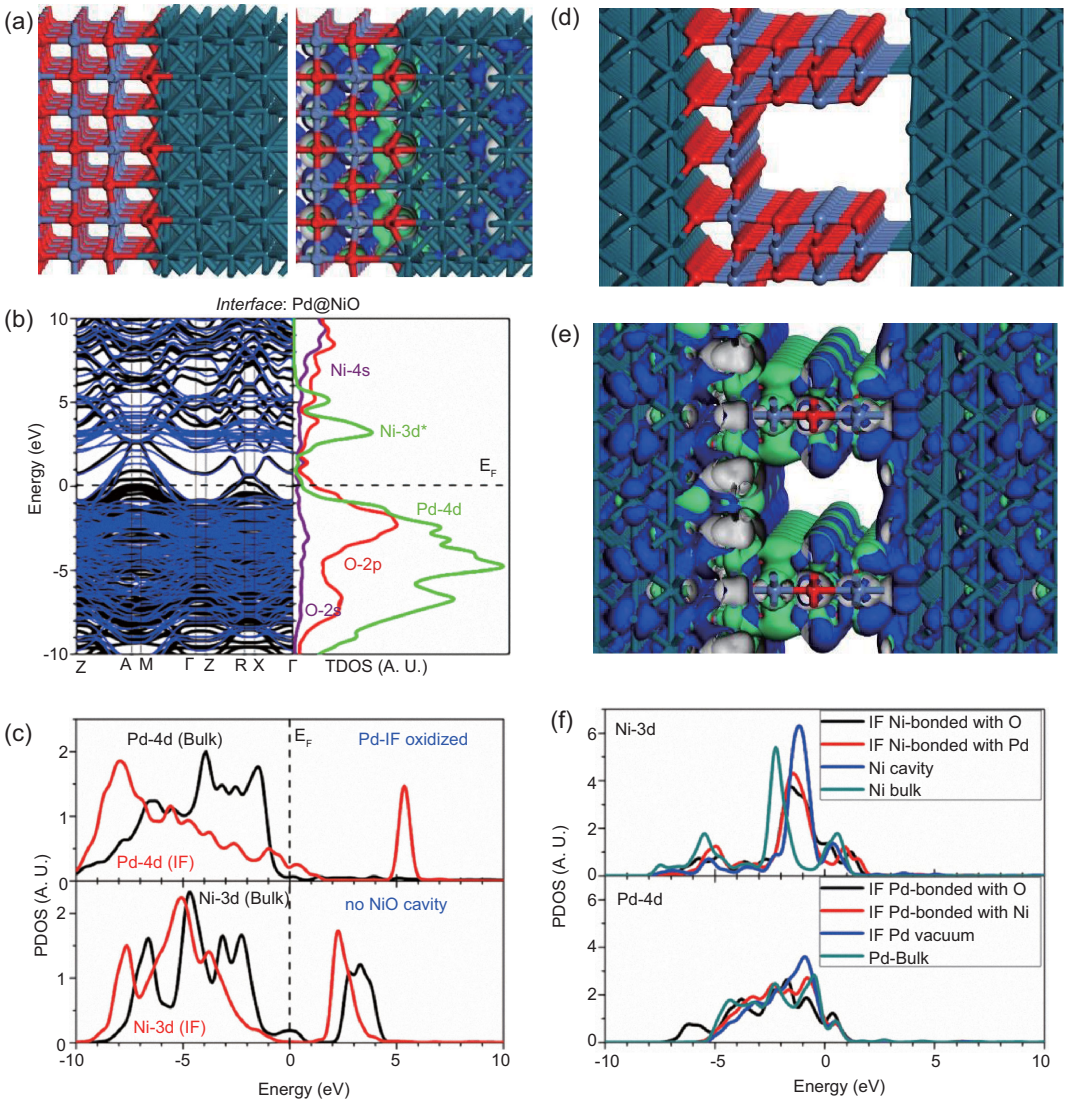

Figure 4. Interface structures and the electronic properties. (a) The local atomic structure and charge densities of bonding and anti-bonding *d*-orbitals of the interface (IF) region, based on cavity-free NiO and Pd (100) fully oxidized. (b) The electronic band structure and total density of states (TDOSs) of the IF model without NiO cavity. (c) The partial density of states (PDOSs) of Pd-*4d* and Ni-*3d* orbital levels from the bulk and IF regions according to the IF model without NiO cavity. (d) The local atomic structure of the IF model with NiO cavity with coexistence of lower-coordinated Pd and Ni sites within the cavity wall. (e) The charge densities of bonding and anti-bonding *d*-orbitals of the cavity region near the IF. (f) The PDOSs of Pd-*4d* and Ni-*3d* orbital levels from different sites in the bulk and those within the cavity region. (Bonding orbital = blue surface, anti-bonding orbital = green surface, Pd = dark green, Ni = light blue, O = red and H = white).

(Fig. 4d). The charge densities of the bonding and anti-bonding orbitals show that the NiO cavity at the IF gives more contrast and directional distribution than the bulk NiO (Fig. 4e). We further investigated the partial density of states (PDOSs) of Ni-3d and Pd-4d orbital levels (Fig. 4f). The Ni-3d-state within the cavity stays at higher levels next to the E_F and possesses the largest weight in the PDOS compared to the Ni-3d at the IF bonded with O or Pd sites, and those in the bulk. Accordingly, the Ni sites within the cavity show relatively higher electronic activity than those from the other regions. Similarly, we also found that the 4d orbital level of the Pd site exposed to the cavity vacuum has the highest peak and weight in the PDOSs. Thus, the Pd exposed to the cavity vacuum and lower-coordinated Ni sites on the cavity wall synchronously match the criteria of the highly selective and direction H_2O_2 synthesis, and can actively adsorb the H_2 and O_2, respectively, without interferences with each other based on the differentiated energy barrier of *d*-electron transfers at the interface.

To understand the related mechanism, we present the evolutions of the transition energy

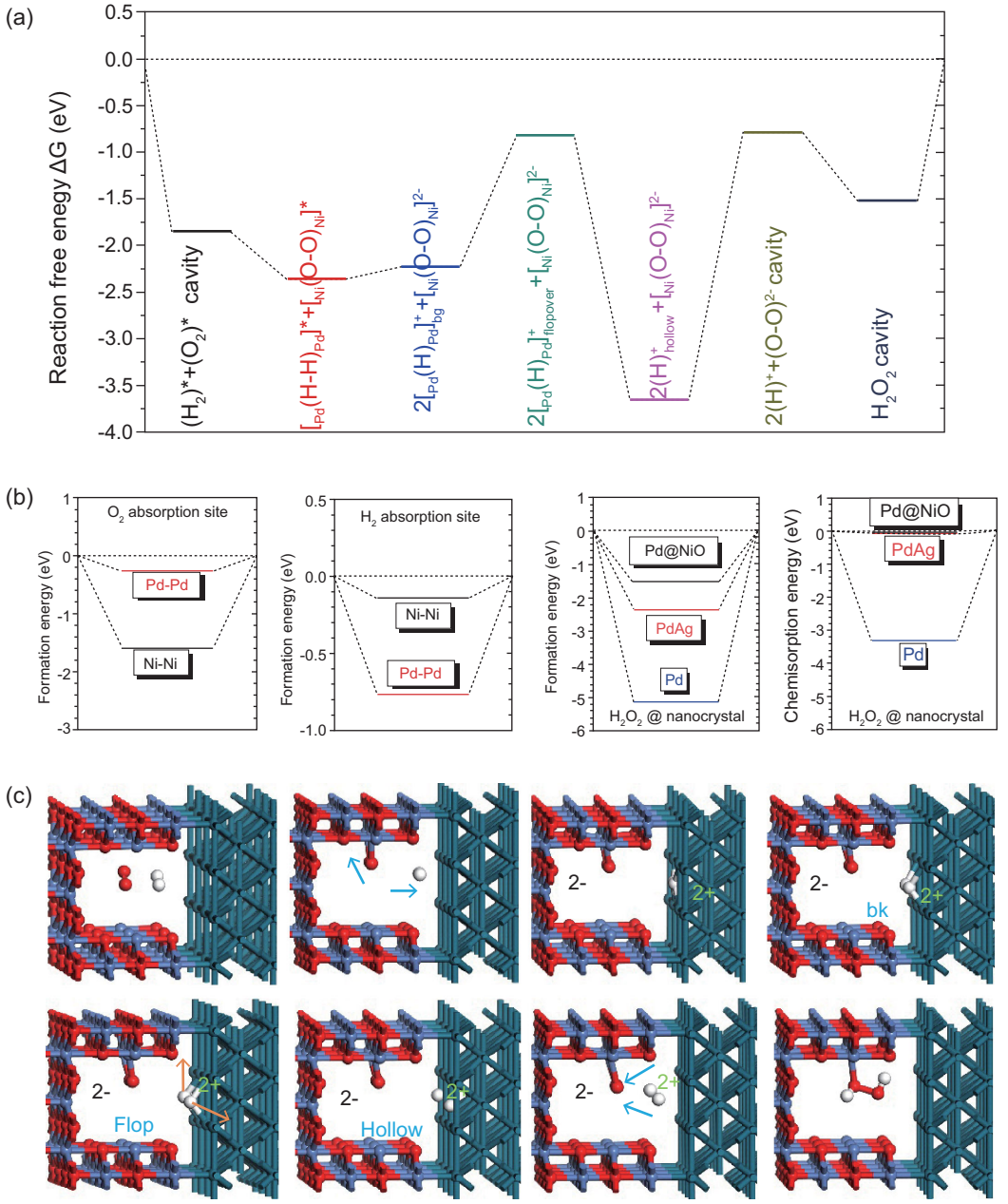

Figure 5. Energy profile for the mechanism. (a) The energy-level diagram of the interpreted reaction regarding the change in free energy simulated within the cavity at the IF region. (b) The formation energies of H_2, O_2 and H_2O_2 within the cavity region, as well as the chemisorption energy of H_2O_2 near the cavity wall at the IF. (c) The local structures and bonding variations of H_2, O_2 and H_2O_2 in the simulation for interpreting the direct synthesis reaction (Pd = dark green, Ni = light blue, O = red and H = white).

profile regarding the aforementioned reaction. The route-map of the synthesis is illustrated in terms of the reaction free energy diagram (ΔG), formation energy and the chemisorption energy, as shown in Fig. 5a and b, respectively. Within this cavity region (Fig. 5c), the most stable configuration for the O_2 location on the cavity wall of the NiO is the bridge-bonding between two adjacent Ni sites, with the O–O bond along the diagonal line of the Ni-O local square motif in the NiO lattice, while this configuration is rather unstable for H_2 as contrasted in the formation energies (Fig. 5b). The H_2 prefers to be adsorbed on the Pd surface that is exposed to the cavity vacuum. In addition, high 4d orbital electronic activity of the lower coordinate Pd site will further induce the bond cleavage of H–H and individually forms of Pd–H–Pd bonding at the bridge site within the Pd square lattice. However, the most stable location for the H is the hollow site on the Pd (100) surface. Spontaneous

evolution of absorption sites of H takes place from the bridge site to the hollow site driven by the energetic downhill process, after the H–H cleavage. The charge transfers for both H and O_2 with the cavity region at the interface are more energetically favorable. With the Coulombic attractive potential, the $2H^+$ will have a fast recombination with O_2^{2-} and react into the H_2O_2 finally. Generally, the energetic interval between the reacting state and the thermoneutral line ($\Delta G = 0$ eV) moderately determines the absorption and desorption abilities of species molecules—the deeper the stronger absorption, but rather weaker in desorption, and vice versa. The direction synthesis of H_2O_2 near the cavity wall within the NiO layer ($\Delta G = -0.048$ eV) shows uniquely high performance to continuously yield H_2O_2 compared with the other alloy systems such as Pd ($\Delta G = -3.30$ eV) or PdAg ($\Delta G = -0.068$ eV). This arises because of the energetic contrast in the formation of energy between the surface and the H_2O_2 molecule. Therefore, the calculation shows that the Pd@porous NiO system has rather high performance for the direct synthesis of H_2O_2 with high selectivity via morphology control on the interface together with an efficient desorption. The superiority in selectivity is achieved by a spontaneous bond scission of H–H and charge transfer from O_2^0 to O_2^{2-} within the cavity of the NiO interfacing with the Pd surface.

CONCLUSIONS

In summary, a unique class of supported Pd@NiO-x core–shell catalysts have been successfully constructed as highly efficient catalysts toward direct H_2O_2 generation. By tuning the catalyst composition and the reaction conditions, the optimized 5 wt% Pd@NiO-3/TiO_2 exhibited high activity, superior selectivity, low degradation activity and excellent stability toward direct H_2O_2 generation. The presence of partially oxidized Pd on the surface of the Pd core as well as the unique NiO shell makes the active Pd core co-modified by oxidized Pd and NiO, which is effective to prevent H_2O formation and guarantees the high selectivity of direct H_2O_2 synthesis. The theoretical investigation revealed that the enhanced performance is due to the cavity-contained unique interface structure between the Pd core and the porous NiO shell, which suppresses the overbinding between the Pd core and $(O–O)^*$ via modifications of the Pd core surface electronic properties. The present work reported here highlights the importance of surface and interface engineering of Pd-based catalysts for direct H_2O_2 synthesis with largely enhanced activity and selectivity.

METHODS

Preparation of Pd@Ni-x core–shell nanoparticles (NPs)

In a typical synthesis of Pd@Ni-3 core–shell NPs, 3.5 mg $Pd(acac)_2$, 7.5 mg $Ni(HCO_2)_2{\cdot}2H_2O$, 36 mg AA, 2.5 mL OAm and 2.5 mL ODE were added into a vial (volume: 30 mL). After the vial had been capped, the mixture was ultrasonicated for around 30 min. The resulting homogeneous mixture was heated from room temperature to 160°C for around 0.5 h and kept at 160°C for 5 h in an oil bath. After cooling to room temperature, the colloidal products were collected by centrifugation and washed three times using cyclohexane/ethanol (v:v = 1:9) mixture. For the synthesis of Pd@Ni-1, Pd@Ni-2 and Pd@Ni-4 core–shell NPs, all the conditions are similar to those of the Pd@Ni-3 core–shell NPs except by changing the dosage of $Ni(HCO_2)_2{\cdot}2H_2O$ to 5, 10 and 12 mg, respectively.

Preparation of 5 wt% Pd@Ni-x/TiO_2 and 5 wt% Pd@NiO-x/TiO_2

In a typical preparation of 5 wt% Pd@Ni-x/TiO_2, the as-prepared Pd@Ni-x core–shell NPs were dispersed in 15 mL chloroform. TiO_2 was then added to the solution with stirring. After stirring for 3 h, the products were collected by centrifugation and dried in 60°C for 5 h. All the catalysts had the Pd loading of 5 wt% unless otherwise stated. The obtained 5 wt% Pd@Ni-x/TiO_2 were then calcined in static air at different temperatures with a ramp rate of 10°C min^{-1} for a desirable time to generate the 5 wt% Pd@NiO-x/TiO_2.

Preparation of 5 wt% Pd/TiO_2

In a typical preparation of 5 wt% Pd/TiO_2, 5 wt% Pd@Ni-3/TiO_2 was dispersed in the diluted HCl solution (20 wt%) and sonicated for 30 min. The products were collected by centrifugation and then washed five times using H_2O.

Catalytic measurements

H_2O_2 synthesis and degradation were performed using a Parr Instruments stainless steel autoclave with a nominal volume of 50 mL and a maximum working pressure of 14 MPa. For the standard H_2O_2 synthesis, the autoclave was charged with the catalyst (0.0025 g unless otherwise stated), solvent (5.6 g MeOH and 2.9 g H_2O, both high performance liquid chromatography (HPLC) grade). The charged autoclave was then purged three times with

O_2 (0.2 MPa) before filling with O_2 to a pressure of 0.4 MPa at room temperature, and then filled with 5% H_2/N_2 (3.6 MPa) at a total pressure of 4.0 MPa. All experiments were carried out at the desired temperature of 2°C and under stirring (1200 rpm) for 30 min unless otherwise stated. The H_2O_2 productivity was determined by titrating aliquots of the final solution with acidified $Ce(SO_4)_2$ (0.01 M) in the presence of two drops of ferroin indicator. The $Ce(SO_4)_2$ solutions were standardized against $(NH_4)_2Fe(SO_4)_2{\cdot}6H_2O$ using ferroin as indicator. Gas analysis was performed by gas chromatography (Shiweipx GC-7806) equipped with a GDX-502 column connected to a thermal conductivity detector. Conversion of H_2 was calculated by gas analysis before and after reaction.

H_2O_2 hydrogenation was carried out in a similar manner to the H_2O_2 synthesis, but in the absence of O_2 in the gas stream and with the presence of varying concentrations of H_2O_2 (2, 4 and 8 wt%) in the solvent (2 wt%: 0.56 g 30 wt% H_2O_2, 2.34 g HPLC water, 5.6 g CH_3OH; 4 wt%: 1.13 g 30 wt% H_2O_2, 1.77 g HPLC water, 5.6 g CH_3OH; 8 wt%: 2.27 g 30 wt% H_2O_2, 0.63 g HPLC water, 5.6 g CH_3OH). The decrease in H_2O_2 concentration (as determined from measurements taken before and after the reaction) is attributed to a combination of H_2O_2 hydrogenation and decomposition. H_2O_2 selectivity was calculated according to the following equation:

$$\text{Selectivity} = (\text{moles of } H_2O_2 \text{ formed}) / (\text{moles of } H_2 \text{ reacted}) \times 100\%$$

Calculations on the Pd-4*d* orbital feature and electronic structures

We used the CASTEP code to perform our DFT+U calculations [34]. In this framework, we used the rotationally invariant (Anisimov-type) DFT+U functional [35] and the Hubbard U parameter self-consistently determined for the pseudized Pd-4*d* and Ni-3*d* orbital by our newly devised two-way crossover linear response method [36,37], which has been already successfully reflecting that the electron–electron Coulomb potential for semi-core orbitals should be considered when using DFT+U [36,37]. The geometry optimization used the Broyden-Fletcher-Goldfarb-Shannon (BFGS) algorithm throughout all calculations.

The PBE functional was chosen for PBE+U calculations with a kinetic cutoff energy of 750 eV, with the valence electron states expressed in a plane-wave basis set. The ensemble DFT (EDFT) method of Marzari *et al.* [38] was used for convergence. The supercell of the *fcc*-Pd (100) surface model was chosen as 3 × 3 × 1 with sizes of 108 atoms (i.e. Pd_{108}) and is established at six layers thick. The vacuum thickness is set to be 15 Å. We only allowed the top two layers to be varied freely. The reciprocal space integration was performed using the mesh of 2 × 2 × 1 with a Gamma-center-off, which was self-consistently selected for total energy minimization [39]. With these special *k*-points, the total energy was converged to less than 5.0×10^{-7} eV per atom. The Hellmann-Feynman forces on the atom are converged to less than 0.001 eV/Å. Since the rocksalt NiO (100) has a relatively small lattice mismatch to the Pd (100), we built the NiO shell layer by choosing the same lattice parameters. To model the cavity area of the as-synthesized porous NiO shell layer, we create a vacant area with a volume of $8.62 \times 6.04 \times 8.62$ (Å^3). This porous NiO shell layer was set to four layers thick. Since the interface model has two faces in bonding, we set the one face of the Pd (100) facing the cavity of the NiO as partially and moderately bonded by O-sites, and the other face as fully oxidized by the O-sites from the NiO shell layer, respectively.

As for the norm-conserving pseudopotentials, these can reflect electron behavior for outer shell valence electrons for |S-matrix| = 1 and provide a better response in DFT+U calculations, especially for the calculations of defects [40–42]. In addition, the almost identical values of the U parameters for both norm-conserving and ultrasoft pseudopotentials obtained in our method indicate that the obtained value has an intrinsic physical meaning for the studied objects. Meanwhile, this will help us to reflect the all-electron behavior of the valence electrons especially for the subtle effect of the 4*d* electrons and outer 5 *s* electrons. The Pd and Ni norm-conserving pseudopotentials were generated using the OPIUM code in the Kleinman-Bylander projector form [43] and the non-linear partial core correction [44] and a scalar relativistic averaging scheme [45] were used to treat the spin-orbital coupling effect. For this treatment, we similarly choose the non-linear core correction technique for correcting the valence-core charge density overlapping in such heavy fermions elements. In particular, the (4*d*, 5 *s*, 5*p*) states were treated as the valence states of both Pd and the (3*d*, 4 *s*, 4*p*) for Ni atoms. The pseudopotentials were optimized by the RRKJ method [46].

Prior to ab-initio predictions of the Hubbard U on orbitals, the PBE functional calculations were used to optimize the geometries and lattice parameters of all Pd and NiO structural models. We used this well-developed pseudopotential technique before Hubbard U determination due to the reliabilty of DFT for the structural optimization of

compound solids even with 4*f* or 5*f* orbitals [37] and ultrasoft pseudopotentials [36,42]. More importantly, as shown by the little difference in the DFT and DFT+U calculated lattice parameters, the electrons on semi-core orbitals can be treated as valence electrons, but the U parameter must be determined more carefully [36,37,42].

With the above preliminary structure determination, the corresponding electronic structure was further estimated using the anisimov-type rotational invariant DFT+U method with the CASTEP code [35]. We previously devised a method to ab-initially determine the semi-core *d*/*f* orbital energy in order to further self-consistently correct the electronic structures from routine first-principles calculations [36,37]. Our work shows that the method is particularly valid for those materials synthesized via extremely physical or chemical conditions [36,37]. The Hubbard U parameter has been self-consistently determined based on our previously developed method [36,37]. For all of the electronic state calculations in the Pd@NiO models, we used self-consistent determination for the U correction on the localized 4d orbitals to correct the on-site Coulomb energy of the electron spurious self-energy. By that method, the Hubbard U parameters on the completely filled shell of $4d^{10}$ orbitals of the Pd was self-consistently determined to be $U_d = 10.13$ eV and $U_d = 5.58$ eV for Ni-$3d^8$. Meanwhile, to stabilize the hole states induced by the O-2*p* orbitals, we self-consistently chose $U_p = 4.23$ eV for O-$2p^4$ orbitals in the anti-ferromagnetic NiO lattice, based on our devised linear response method [36,37]. With our self-consistent determination process, the on-site Hubbard U potential parameters for the Pd-4*d*, Ni-3*d* and O-2*p* orbitals have been determined in Supplementary Fig. 10, available as Supplementary Data at *NSR* online.

SUPPLEMENTARY DATA

Supplementary data are available at *NSR* online.

ACKNOWLEDGEMENTS

The characterizations were made at the Testing & Analysis Center in Soochow University.

FUNDING

This work was financially supported by the Ministry of Science and Technology of China (2016YFA0204100, 2017YFA0208200), the National Natural Science Foundation of China (21571135), Young Thousand Talented Program, Jiangsu Province Natural Science Fund for Distinguished Young Scholars (BK20170003), the Project of Scientific and Technologic Infrastructure of Suzhou (SZS201708), the start-up supports from Soochow University and the Priority Academic Program Development of Jiangsu Higher Education Institutions (PAPD).

Conflict of interest statement. None declared.

REFERENCES

1. Campos-Martin JM, Blanco-Brieva G and Fierro JL *et al.* Hydrogen peroxide synthesis: an outlook beyond the anthraquinone process. *Angew Chem Int Ed* 2006; **45**: 6962–84.
2. Myers RL. *The 100 Most Important Chemical Compounds: a Reference Guide*. Westport, CT: Greenwood Publishing Group, 2007.
3. Hage R and Lienke A. Applications of transition-metal catalysts to textile and wood-pulp bleaching. *Angew Chem Int Ed* 2006; **45**: 206–22.
4. Yi Y, Wang L and Li G *et al.* A review on research progress in the direct synthesis of hydrogen peroxide from hydrogen and oxygen: noble-metal catalytic method, fuel-cell method and plasma method. *Catal Sci Technol* 2016; **6**: 1593–610.
5. Kamata K, Yonehara K and Sumida Y *et al.* Efficient epoxidation of olefins with >=99% selectivity and use of hydrogen peroxide. *Science* 2003; **300**: 964–6.
6. Van WJ, Schoebrechts JP and Colery JC. *U.S. Patent* 1992; 5447706.
7. Edwards JK and Hutchings GJ. Palladium and gold-palladium catalysts for the direct synthesis of hydrogen peroxide. *Angew Chem Int Ed* 2008; **47**: 9192–8.
8. Edwards JK, Freakley SJ and Carley AF *et al.* Strategies for designing supported gold-palladium bimetallic catalysts for the direct synthesis of hydrogen peroxide. *Acc Chem Res* 2014; **47**: 845–54.
9. Lari GM, Puértolas B and Shahrokhi M *et al.* Hybrid palladium nanoparticles for direct hydrogen peroxide synthesis: the key role of the ligand. *Angew Chem Int Ed* 2017; **56**: 1775–9.
10. Xu H, Cheng D and Gao Y *et al.* Design of high-performance Pd-based alloy nanocatalysts for direct synthesis of H_2O_2. *ACS Catal* 2017; **7**: 2164–70.
11. Wilson NM and Flaherty DW. Mechanism for the direct synthesis of H_2O_2 on Pd clusters: heterolytic reaction pathways at the liquid-solid interface. *J Am Chem Soc* 2016; **138**: 574–86.
12. Edwards JK, Solsona B and Carley AF *et al.* Switching off hydrogen peroxide hydrogenation in the direct synthesis process. *Science* 2009; **323**: 1037–41.
13. Sankar M, He Q and Morad M *et al.* Synthesis of stable ligand-free gold-palladium nanoparticles using a simple excess anion method. *ACS Nano* 2012; **6**: 6600–13.
14. Hutchings GJ and Kiely CJ. Strategies for the synthesis of supported gold palladium nanoparticles with controlled morphology and composition. *Acc Chem Res* 2013; **46**: 1759–72.
15. Chen M, Kumar D and Yi C *et al.* The promotional effect of gold in catalysis by palladium-gold. *Science* 2005; **310**: 291–3.
16. Liu Q, Bauer JC and Schaak RE *et al.* Direct synthesis of H_2O_2 from H_2 and O_2 over Pd-Pt/SiO_2 bimetallic catalysts in a H_2SO_4/ethanol system. *Appl Catal A Gen* 2008; **339**: 130–6.

17. Xu J, Ouyang L and Da GJ *et al.* Pt promotional effects on Pd-Pt alloy catalysts for hydrogen peroxide synthesis directly from hydrogen and oxygen. *J Catal* 2012; **285**: 74–82.
18. Edward JK, Pritchard J and Lu L *et al.* The direct synthesis of hydrogen peroxide using platinum-promoted gold-palladium catalysts. *Angew Chem Int Ed* 2014; **53**: 2381–4.
19. Gu J, Wang S and He Z *et al.* Direct synthesis of hydrogen peroxide from hydrogen and oxygen over activated-carbon-supported Pd-Ag alloy catalysts. *Catal Sci Technol* 2016; **6**: 809–17.
20. Ntainjua EN, Freakley SJ and Hutchings GJ. Direct synthesis of hydrogen peroxide using ruthenium catalysts. *Top Catal* 2012; **55**: 718–22.
21. Freakley SJ, He Q and Harrhy JH *et al.* Palladium-tin catalysts for the direct synthesis of H_2O_2 with high selectivity. *Science* 2016; **351**: 965–8.
22. Plauck A, Stangland EE and Dumesic JA *et al.* Active sites and mechanisms for H_2O_2 decomposition over Pd catalysts. *Proc Natl Acad Sci USA* 2016; **113**: E1973–82.
23. Dissanayake DP and Lunsford JH. The direct formation of H_2O_2 from H_2 and O_2 over colloidal palladium. *J Catal* 2003; **214**: 113–20.
24. Li Q, Fu J and Zhu W. Tuning Sn-catalysis for electrochemical reduction of CO_2 to CO via the core/shell Cu/SnO_2 structure. *J Am Chem Soc* 2017; **139**: 4290–3.
25. Huang R, Wen YH and Shao GF *et al.* Atomic structure and thermal stability of Pt-Fe bimetallic nanoparticles: from alloy to core/shell architectures. *Phys Chem Chem Phys* 2016; **18**: 17010–7.
26. Guo W, Sun W and Zhu J *et al.* Multilayer CuO@NiO hollow spheres: microwave-assisted metal-organic-framework derivation and highly reversible structure-matched stepwise lithium storage. *ACS Nano* 2015; **9**: 11462–71.
27. Yang Z, Xu F and Zhang W *et al.* Controllable preparation of multishelled NiO hollow nanospheres via layer-by-layer self-assembly for supercapacitor application. *J Power Sources* 2014; **246**: 24–31.
28. Yuan C, Wu HB and Xie Y *et al.* Mixed transition-metal oxides: design, synthesis, and energy-related applications. *Angew Chem Int Ed* 2014; **53**: 1488–504.
29. Railback JG, Johnston-Peck AC and Wang J *et al.* Size-dependent nanoscale Kirkendall effect during the oxidation of nickel nanoparticles. *ACS Nano* 2010; **4**: 1913–20.
30. Gonzalez E, Arbiol J and Puntes VF *et al.* Carving at the nanoscale: sequential galvanic exchange and Kirkendall growth at room temperature. *Science* 2011; **334**: 1377–80.
31. Wang Q, Chen S and Shi F *et al.* Structural evolution of solid Pt nanoparticles to a hollow PtFe alloy with a Pt-skin surface via space-confined pyrolysis and the nanoscale Kirkendall effect. *Adv Mater* 2016; **28**: 10673–8.
32. Yin YD, Rioux RM and Erdonmez CK *et al.* Formation of hollow nanocrystals through the nanoscale Kirkendall effect. *Science* 2004; **304**: 711–4.
33. Niu KY, Park J and Zheng H *et al.* Revealing bismuth oxide hollow nanoparticle formation by the Kirkendall effect. *Nano Lett* 2013; **13**: 5715–9.
34. Clark SJ, Segall MD and Pickard CJ *et al.* First principles methods using CASTEP. *Zeitschrift Fur Kristallographie* 2005; **220**: 567–70.
35. Vladimir IA, Aryasetiawan F and Lichtenstein AI *et al.* First-principles calculations of the electronic structure and spectra of strongly correlated systems: the LDA + U method. *J Phys Condens Matter* 1997; **9**: 767–808.
36. Huang B. 4f fine-structure levels as the dominant error in the electronic structures of binary lanthanide oxides. *J Comput Chem* 2016; **37**: 825–35.
37. Huang B. The screened pseudo-charge repulsive potential in perturbed orbitals for band calculations by DFT+U. *Phys Chem Chem Phys* 2017; **19**: 8008–25.
38. Marzari N, Vanderbilt D and Payne MC *et al.* Ensemble density-functional theory for Ab initio molecular dynamics of metals and finite-temperature insulators. *Phys Rev Lett* 1997; **79**: 1337–40.
39. Probert MIJ. Improving the convergence of defect calculations in supercells: an ab initio study of the neutral silicon vacancy. *Phys Rev B* 2003; **67**: 075204.
40. Hasnip PJ and Pickard CJ. Electronic energy minimisation with ultrasoft pseudopotentials. *Comput Phys Commun* 2006; **174**: 24–9.
41. Laasonen K, Pasquarello A and Car R. Car-Parrinello molecular dynamics with Vanderbilt ultrasoft pseudopotentials. *Phys Rev B* 1993; **47**: 10142–53.
42. Huang B, Gillen R and Robertson J *et al.* Study of CeO_2 and its native defects by density functional theory with repulsive potential. *J Phys Chem C* 2014; **118**: 24248–56.
43. Kleinman L and Bylander DM. Efficacious form for model pseudopotentials. *Phys Rev Lett* 1982; **48**: 1425–8.
44. Louie SG, Froyen S and Cohen ML *et al.* Nonlinear ionic pseudopotentials in spin-density-functional calculations. *Phys Rev B* 1982; **26**: 1738–42.
45. Grinberg I, Ramer NJ and Rappe AM *et al.* Transferable relativistic Dirac-Slater pseudopotentials. *Phys Rev B* 2000; **62**: 2311–4.
46. Rappe AM, Rabe KM and Kaxiras E *et al.* Optimized pseudopotentials. *Phys Rev B* 1990; **41**: 1227–30.